Multi-Wavelength Pulse Generation Using Narrow-Gap Topological Crystalline Insulator $Pb_{1-X}Sn_XTe$

Siyu Li, Xin Xie, Xuefen Kan, Yan Lu [ID], Qiang Yu [ID], Xinxin Zhao, Cheng Yin, and Xianping Wang [ID]

Abstract—A multi-wavelength pulse is generated using chemical vapor deposition method (CVD) to fabricate the topological crystalline insulator (TCI) $Pb_{1-X}Sn_XTe$ as a saturated absorber (SA). Compared with other SA materials, $Pb_{1-X}Sn_XTe$ have advantages of narrow bandgap and high optical absorption in the near-infrared region. The laser produced a stable four-wavelength lasing configuration characterized by a wavelength spacing of approximately 2 nm, with pulse duration, repetition rate, and signal-to-noise ratio (SNR) of 0.899 to 0.854 μs, 1.08 to 1.15 MHz, and 31.5 dB, respectively. The results indicate that the $Pb_{1-X}Sn_XTe$-SA is suitable for pulsed generation in the near-infrared region and its potential in various fields, including super-resolution imaging, high-density optical storage, and three-dimensional laser lithography.

Index Terms—$Pb_{1-X}Sn_XTe$, saturable absorber, topological crystalline insulator, pulse laser.

P ULSED lasers play a significant role in many applications, such as optical frequency measurements [1], ranging metrology [2], and laser surgery medical applications [3]. There are two main operating modes of lasers: Q-switching and mode-locking, which can be implemented actively or passively. Passive implementations lasers are highly favored for their simplicity, affordability, and compactness. These implementations can be achieved by utilizing either artificial or real saturable absorbers (SAs). Although artificial SAs offer simplicity and compactness, their performance is susceptible to the influence of environmental conditions. Conversely, real SAs present a cost-effective and straightforward solution for fiber laser cavities. They can be effortlessly integrated and provide enhanced environmental stability compared to their artificial counterparts. Several real SAs have been reported in the literature, such as graphene [4], transition metal dichalcogenides (TMDs) [5], rare earth oxide [6] and topological insulators (TIs) [7] have been demonstrated as effective optical modulator in passively pulsed lasers.

The potential of $Pb_{1-X}Sn_XTe$ as a material for saturable absorbers (SAs) in pulse lasers remains unexplored, despite its adjustable bandgap, wide spectral range, and rapid response time. $Pb_{1-X}Sn_XTe$ is a topological crystalline insulator (TCI) that exhibits spatial symmetry rather than temporal inversion symmetry, resulting in greater robustness and reliability. Its surface states are stabilized by point group symmetry [8]. Previous studies have primarily focused on investigating the electrical transport [9], magnetic physics [10], and thermoelectric effect [11] of $Pb_{1-X}Sn_XTe$ with a cubic crystal structure. However, its application in pulse lasers has not been explored. $Pb_{1-X}Sn_XTe$ functions as a TCI, which means its carrier recovery time is typically in the picosecond range, making it suitable for generating Q-switched laser pulses. Additionally, the carrier relaxation time of $Pb_{1-X}Sn_XTe$-SA can be modulated, allowing for feasible mode-locking operation. While conventional topological insulators (TIs) exhibit 2D anisotropic growth due to their layered crystal structure, TCIs lack intrinsic motivation for 2D geometry growth due to their rock-salt architecture [12]. However, by optimizing experimental conditions such as growth temperature and substrate surface chemical properties, 2D anisotropic growth can be induced in TCIs through chemical activity differences between crystal planes [13].

In this letter, $Pb_{1-X}Sn_XTe$ nanosheets were synthesized on mica substrates using the chemical vapor deposition (CVD) method. To facilitate non-destructive transfer of $Pb_{1-X}Sn_XTe$ samples, we utilized polydimethylsiloxane (PDMS) as the transfer medium. The resulting multi-wavelength pulse based on $Pb_{1-X}Sn_XTe$-SA demonstrated a wavelength spectral bandwidth of approximately 2nm. Overall, the results have explored the potential of $Pb_{1-X}Sn_XTe$ as a material for saturable absorbers in pulse lasers, highlighting its unique properties as a topological crystalline insulator. By synthesizing $Pb_{1-X}Sn_XTe$ nanosheets and utilizing PDMS for transfer, we have successfully generated a multi-wavelength pulse with a narrow wavelength spectral bandwidth. the findings pave the way for further research and development of $Pb_{1-X}Sn_XTe$-SA in laser applications.

Siyu Li, Xin Xie, and Xianping Wang are with the Jiangxi Key Laboratory of Photoelectronics and Telecommunication, College of Physics and Communication Electronics, Jiangxi Normal University, Nanchang 330022, China (e-mail: 202026002028@jxnu.edu.cn; xxinoptics@yeah.net; xpwang@jxnu.edu.cn).

Xuefen Kan and Yan Lu are with the School of Transportation Engineering, Jiangsu Shipping College, Nantong 226010, China (e-mail: kanxf@jssc.edu.cn; luyan@jssc.edu.cn).

Qiang Yu is with the CAS Key Laboratory of Nanophotonic Materials and Devices & Key Laboratory of Nanodevices and Applications, i-Lab, Suzhou Institute of Nano-Tech and Nano-Bionics, Chinese Academy of Sciences, Suzhou 215123, China (e-mail: qyu2015@sinano.ac.cn).

Xinxin Zhao is with the Institute of Energy, Hefei Comprehensive National Science Center, Hefei 230031, China (e-mail: zhaoxx@ie.ah.cn).

Cheng Yin is with the Key Laboratory of Power Transmission and Distribution Equipment Technology, Hohai University, Changzhou 213022, China (e-mail: 20111851@hhu.edu.cn).

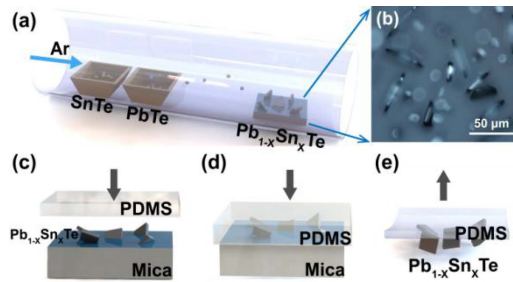Digital Object Identifier 10.1109/JPHOT.2023.3313983

Fig. 1. Synthesis, exfoliation, and transferring process of $Pb_{1-x}Sn_xTe$ nanosheets. (a) Chemical vapor deposition process. (b) Optical microscope image of the $Pb_{1-X}Sn_XTe$ nanosheets. (c)–(e) The transferring process using PDMS.

Fig. 2. Schematic diagram of the ring cavity of the fiber laser with $Pb_{1-X}Sn_XTe$-SA. LD, 980 nm laser diode; WDM, wavelength division multiplexer; EDF, erbium-doped fiber; PC, polarization controller; ISO, polarization-independent isolator; $Pb_{1-x}Sn_xTe$-SA; OC, output coupler.

The synthesis progress of 2D $Pb_{1-X}Sn_XTe$ nanosheets involved several steps. Firstly, the layered mica was chosen as the substrate for the growth of $Pb_{1-X}Sn_XTe$, because fluorophlogopite mica possesses a pseudo-hexagonal Z_2O_5 (Z = Si, Al) layered structure with space group C12/m1 and exhibits remarkable stability against light, electricity, moisture, and high temperature due to weak van der Waals interactions at the interface of the adjacent layer [14], which enables facile mechanical cleavage into flexible transparent thin flakes with an exposed surface {001}. Secondly, the SnTe and PbTe powders were converted into $Pb_{1-X}Sn_XTe$ nanosheets via the CVD method, as shown in Fig. 1(a). In a single temperature zone horizontal tube furnace, 0.2 g SnTe and 0.2 g PbTe powders were placed in the upstream with distance from the center, while fluorophlogopite mica sheets were added downstream at a distance of 10–15 cm from the center of the tube. Then quartz tube was flushed by Ar gas a few times. Setting the growth temperatures to 640–690 °C and Ar gas was fed with a constant flow rate 20 sccm. The whole reaction duration maintains 2–5 min. After that, the furnace naturally cooled down to room temperature. The optical diagram in Fig. 1(b) shows the $Pb_{1-X}Sn_XTe$ nanosheets with thickness mainly distributing in 40 nm and lateral dimension as large as 20 μm at a source temperature of 650 °C.

The atomic structure model of $Pb_{1-X}Sn_XTe$ is shown in Fig. S1(a), and S2(b) demonstrates the highly single-crystalline nature of the $Pb_{1-X}Sn_XTe$ nanoplate through well-defined lattice fringes. The presence of perfect cubic patterns confirms the highly symmetrical rock-salt structure of $Pb_{1-X}Sn_XTe$. The high-angle annular dark-field (HAADF) imaging further reveals lattice points with a crystal plane spacing of approximately 0.33 nm. Energy-dispersive spectroscopy (EDS) was then conducted to analyze the elemental distribution in the $Pb_{1-X}Sn_XTe$ nanosheets, as depicted in Fig. S1(c–f). The EDS analysis confirms the homogeneity of the nanosheets, with an atomic ratio of (Pb/Sn)/Te approximately 1:1 within the experimental error range.

To gain further insight into the electronic properties of $Pb_{1-X}Sn_XTe$ nanosheets, the band structures and density of states (DOS) were computed by vienna Ab initio simulation package (VASP), as shown in Fig. S2. The analysis reveals a band gap of 0.21 eV at the Γ point, with the conduction band minimum (CBM) and valence band maximum (VBM) located at 0.12 eV and -0.09 eV, respectively. Notably, the p orbitals,
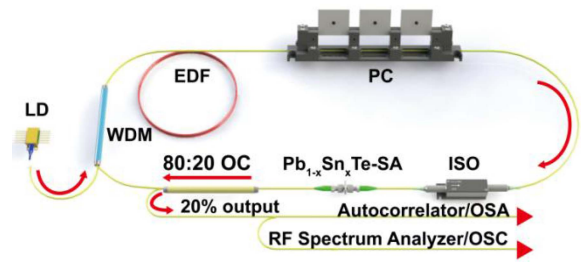
which have a larger electron cloud radius due to the presence of P element, significantly influence the vicinity of the Fermi surface and play a crucial role in chemical bonding by forming covalent bonds. Conversely, the s and d orbitals have negligible effects on the system. In summary, these findings confirm that $Pb_{1-X}Sn_XTe$ is a narrow-gap semiconductor. Specifically, the saturable absorption process of $Pb_{1-X}Sn_XTe$-SA can be explained by the Pauli blocking principle, wherein weak-intensity light illuminating the material results in photon-generated hot carriers that quickly cool down and suppress inter-band photon transition. However, with stronger light intensity, these carriers occupy energy states near the conduction and valence band edges, resulting in complete Pauli blocking. Consequently, the photons pass through without loss.

To prepare an SA-based optical device, PDMS was used as a transfer medium to transfer the $Pb_{1-X}Sn_XTe$ nanosheets onto the end of the optical fiber, as shown in Fig. 1(c)–(e). Mechanical stripping of PDMS materials resulted in numerous exfoliated $Pb_{1-X}Sn_XTe$ nanosheets. Optical microscopy was then employed to select the thinner nanosheets attached to PDMS materials, which were subsequently sandwiched between two ferrules to create the SA device. The reproducibility of saturable absorbers is a notable feature. The precise transfer of flakes onto the fiber's end face allows for the realization of saturable absorption. Moreover, the material's excellent stability enables the generation of pulses over a prolonged period of time.

Fig. 2 illustrates the schematic diagram of a ring cavity fiber laser that operates at 1500 nm using $Pb_{1-X}Sn_XTe$ as the saturable absorber. The laser setup includes a ring cavity configuration and utilizes a 980 nm pump light, which is coupled into the system through a 980/1550 wavelength division multiplexing (WDM) coupler. The gain medium in the cavity is a single-mode erbium-doped fiber (EDF) with a length of 2 m. The EDF has specific characteristics, such as a core diameter of 4 μm, a cladding diameter of 125 μm, a numerical aperture of 0.16, a group velocity dispersion of 27.6 ps^2/km, and an erbium ion absorption of 23 dB/m at 980 nm. The polarization controller (PC) is used to optimize the cavity birefringence, while an optical isolator (ISO) is connected to the PC to prevent backward reflection. The SA device is attached to the other end of the ISO. An optical coupler with an 80:20 ratio is employed to extract 20% of the laser output, while the remaining 80% circulates within the cavity. Various instruments, including a
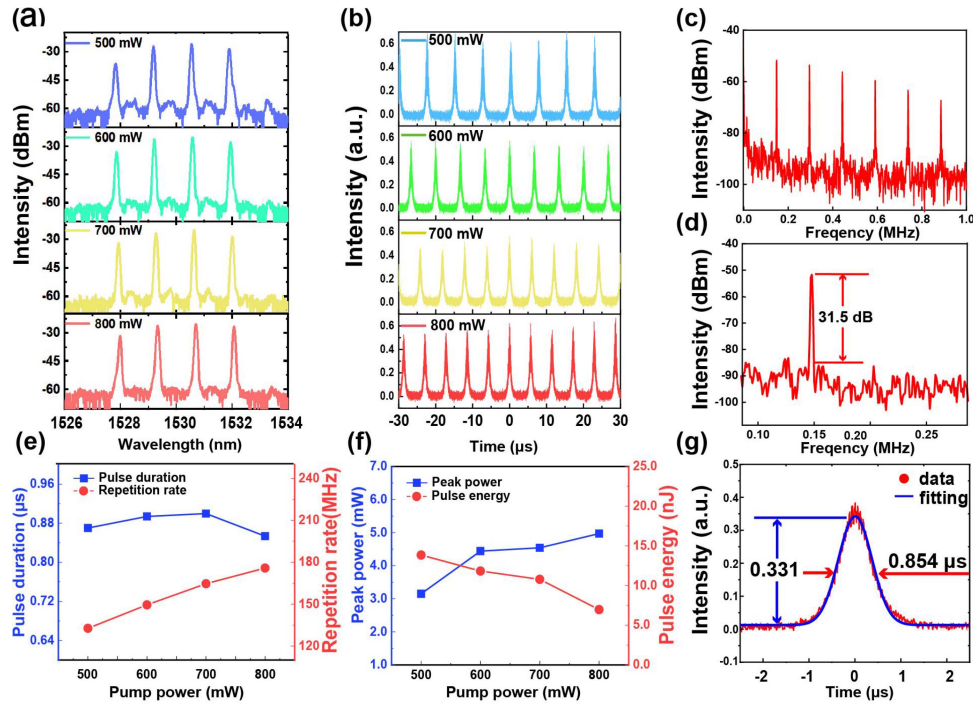
Fig. 3. Performance of multi-wavelength pulse laser based on the Pb$_{1-x}$Sn$_x$Te-SA. (a) The output laser spectra with different pump power (b) pulse sequence at different values of pump power (c) radio frequency spectrum within 1000 KHz range (d) radio frequency spectrum (e) pulse duration and repetition rate versus pump power (f) peak power and pulse energy versus pump power (g) pulse profile at pump power of 800 mW.

highly sensitive autocorrelator, an optical spectrum analyzer (OSA), a radio frequency (RF) spectrum analyzer, and a digital oscilloscope (OSC), are utilized to measure the picosecond pulse width, output wavelength, output pulse train, and record the RF spectrum of the laser, respectively.

After inserting the Pb$_{1-X}$Sn$_X$Te nanosheets into the laser cavity, we conducted experiments to observe the laser performance. Initially, when the pump power was increased gradually from 0 mW to 800 mW and the polarization controller (PC) was adjusted, we only observed continuous wave phenomena (not shown). However, once the Pb$_{1-X}$Sn$_X$Te saturable absorber was inserted, stable pulse laser operation was achieved at a threshold pump power of 400 mW, despite the relatively long cavity length. By further increasing the pump power and fine-tuning the PCs, we were able to optimize the performance of the stable pulse laser generated by the Pb$_{1-X}$Sn$_X$Te saturable absorber, as shown in Fig. 3.

The modulation observed in the optical spectrum is caused by Fabry-Perot interference within the thick glass substrate supporting the metasurface device [15]. In Fig. 3(a), pulse-shaped spectra are shown, obtained by varying the pump power from 500 to 800 mW. These spectra provide strong evidence of stable lasing behavior, with four distinct wavelengths and an approximate spacing of 2 nm. The Fabry-Perot interference arises from a 530 μm gap between the two fiber facets positioned face-to-face, leading to the generation of multiple longitudinal modes within the laser cavity and resulting in the emission of a wide range of wavelengths. Fig. 3(b) illustrates the pulse sequence evolution under different pump power, exhibiting a well-matched pulse separation of 5.72 to 7.56 μs to the length of the designed cavity and a well-distributed pulse amplitude. Furthermore, as

the pump power increases, both the pulse period and width gradually decrease. In Fig. 3(c) indicates the radio frequency spectrum, with the scanning range of 1MHz, which serves to show that no spurious sideband was found within this range, thus indicating the high spectral purity of the laser. The stability of the pulsed laser was investigated based on the RF spectrum obtained at 500 mW pump power, and the fundamental frequency of 148 kHz with 6 harmonics was found to be consistent with the pulse period obtained through the trace of the oscilloscope. Additionally, the RF spectrum exhibited a signal-to-noise ratio (SNR) of 31.5 dB measured at resolution bandwidth (RBW) of 30 Hz, as shown in Fig. 3(d).

According to the data depicted in Fig. 3(e), a noticeable correlation can be observed between the pulse width and the pump power. As the pump power increases from 500 mW to 800 mW, the pulse width also increases from 0.85 μs to 0.89 μs. However, an interesting reversal occurs within the pump power range of 700 mW to 800 mW, where the pulse width drops to 0.85 μs. This pattern suggests that at lower power levels, the pulse width expands with increasing pump power, possibly due to nonlinear optical effects or saturation effects of the optical devices. However, in the higher power range, we observe a trend towards smaller pulse widths. This unusual phenomenon may be attributed to other factors, such as nonlinear optical effects caused by optical loss or high pump light intensity. At the same time, it was observed that with the increase of pump power from 500 mW to 800 mW, the repetition frequency showed a increase trend, from 132.70 KHz to 175.86 KHz. This increasing trend can be explained by the higher response speed of the optical device resulting from the increase in pump power. In optical devices, the augmentation of pump power leads to

TABLE I
ULTRAFAST PULSED LASERS BASED ON DIFFERENT SAS

Materials	Wavelength (nm)	Pulse width (μs)	Repetition Rate (kHz)	Pulse Energy (nJ)	Pump power (mW)	Output power (mW)	Ref.
Graphene	1566.17	3.7	65.9	16.7	6.5-82.8	1.1	[16]
BP	1562.87	10.32	15.78	94.3	50-195	~1.5	[17]
Bi_2Se_3	1565.14	13.4	12.88	15	41.3-84.3	~0.145	[18]
Fe_3O_4	1562.4	2.7	80	78.2	80-342	6.23	[19]
$Pb_{1-x}Sn_xTe$	1527.83-1532.1	0.854-0.899	132.70-175.86	7.09-13.84	500-800	1.25-1.84	This work

a greater number of excited photons, thereby increasing the frequency of optical effects. Consequently, the repetition rate increases with the increment of pump power, indicating the enhanced response speed of the optical device to the pump light.

As shown in Fig. (f), the impact of pump power on the peak power and pulse width energy was examined across the range of 500 mW to 800 mW. It was observed that the peak power experienced a substantial increase from 3.15 mW to 4.97 mW with the increment of pump power. This finding suggests a heightened responsiveness of the optical device to higher pump powers, resulting in enhanced power amplification. Moreover, the pulse width energy demonstrated a decrease from 13.84 nJ to 7.09 nJ as the pump power rose from 500 mW to 800 mW. This decline in pulse width energy implies that the optical device achieves faster response times under higher pump power conditions.

Table I demonstrates the output performances of multi-wavelength pulse laser to compare the nonlinear optical response of $Pb_{1-X}Sn_XTe$-SA with the same kind of SAs using other 2D materials. The relatively high SNR and output power show that the $Pb_{1-x}Sn_xTe$-based SA is suitable for building stable Q-switched fiber lasers and thus for short-pulse generation in the mid-IR wavelength region. Narrow-gap semiconductor $Pb_{1-X}Sn_XTe$ enriches the family of TCI material-based ultrafast lasers, exhibiting broad spectral bandwidth and satisfactory overall performance. In short, our results show superior advantages over previous SAs in terms of pulse width and pulse repetition rate, and $Pb_{1-X}Sn_XTe$ is a valuable and promising material for advanced photonics and optical communication technologies.

In conclusion, $Pb_{1-x}Sn_xTe$ nanosheets were synthesized using the CVD method, and the $Pb_{1-x}Sn_xTe$-SA was manufactured and investigated with nonlinear absorption properties in the communication band. Subsequently, the $Pb_{1-x}Sn_xTe$-SA was integrated into an EDF laser cavity for pulse generation. By adjusting the pump power in the range of 500 to 800 mW, the laser pulses with center wavelength of 1527.83 to 1532.10 nm. Additionally, the repetition frequency and pulse width modulation range were observed as 1.08 to 1.15 MHz and 0.854t o 0.899 μs, respectively. These findings provide strong evidence for the potential of Pb1−xSnxTe-SA in ultrafast photonics applications.

REFERENCES

[1] M. Malinowski et al., "Towards on-chip self-referenced frequency-comb sources based on semiconductor mode-locked lasers," *Micromachines*, vol. 10, no. 6, 2019, Art. no. 391.

[2] H. M. Hussein, O. Terra, H. Hussein, and M. Medhat, "Collinear versus non-collinear autocorrelation between femtosecond pulses for absolute distance measurement," *Measurement*, vol. 152, 2020, Art. no. 107319.

[3] E. Mottay, "Ultrafast pulse lasers in medical applications," *Ind. Laser Solutions*, vol. 28, no. 6, pp. 28–29, 2013.

[4] J. L. Xu, X. L. Li, Y. Z. Wu, X. P. Hao, J. L. He, and K. J. Yang, "Graphene saturable absorber mirror for ultra-fast-pulse solid-state laser," *Opt. Lett.*, vol. 36, no. 10, pp. 1948–1950, 2011.

[5] Q. Yu et al., "Lab-on-fiber based on optimized gallium selenide for femtosecond mode-locked lasers and fiber-compatible photodetectors," *Adv. Photon. Res.*, vol. 4, no. 4, 2023, Art. no. 2200283.

[6] N. Zulkipli et al., "Yttrium oxide (Y2O3) as a pulse initiator in a mode-locking erbium-doped fiber laser," *Photonics*, vol. 9, no. 7, 2022, Art. no. 486.

[7] H. Deng et al., "Mode-locking pulse generation based on lead-free halide perovskite CsCu $_2I_3$ micro-rods with high stability," *J. Mater. Chem. C*, vol. 11, no. 5, pp. 1696–1730, 2023.

[8] Y. Ando and L. Fu, "Topological crystalline insulators and topological superconductors: From concepts to materials," *Annu. Rev. Condens. Matter Phys.*, vol. 6, no. 1, pp. 361–381, 2015.

[9] Q. Wang et al., "Rational design of ultralarge $Pb_{1-x}Sn_xTe$ nanoplates for exploring crystalline symmetry-protected topological transport," *Adv. Mater.*, vol. 28, no. 4, pp. 617–623, 2016.

[10] S.-Y. Xu et al., "Observation of a topological crystalline insulator phase and topological phase transition in $Pb_{1-x}Sn_xTe$," *Nature Commun.*, vol. 3, no. 1, 2012, Art. no. 1192.

[11] I. Sur, A. Casian, V. Kantser, and Z. Dashevsky, "Thermoelectric properties of $Pb_{1-x}Sn_xTe/PbTe$ quantum well structures," *Moldavian J. Phys. Sci.*, vol. 4, no. 4, pp. 449–453, 2005.

[12] Z. Li, S. Shao, N. Li, K. McCall, J. Wang, and S. Zhang, "Single crystalline nanostructures of topological crystalline insulator SnTe with distinct facets and morphologies," *Nano Lett.*, vol. 13, no. 11, pp. 5443–5448, 2013.

[13] H. Li et al., "Controlled synthesis of topological insulator nanoplate arrays on mica," *J. Amer. Chem. Soc.*, vol. 134, no. 14, pp. 6132–6135, 2012.

[14] T. Van Khai et al., "Synthesis and characterization of single-and few-layer mica nanosheets by the microwave-assisted solvothermal approach," *Nanotechnology*, vol. 24, no. 14, 2013, Art. no. 145602.

[15] W. Jia et al., "Intracavity spatiotemporal metasurfaces," *Adv. Photon.*, vol. 5, no. 2, 2023, Art. no. 026002-5.

[16] Z. Luo et al., "Graphene-based passively Q-switched dual-wavelength erbium-doped fiber laser," *Opt. Lett.*, vol. 35, no. 21, pp. 3709–3711, 2010.

[17] Y. Chen et al., "Mechanically exfoliated black phosphorus as a new saturable absorber for both Q-switching and mode-locking laser operation," *Opt. Exp.*, vol. 23, no. 10, pp. 12823–12833, 2015.

[18] Y. Chen et al., "Self-assembled topological insulator: Bi_2Se_3 membrane as a passive Q-switcher in an erbium-doped fiber laser," *J. Lightw. Technol.*, vol. 31, no. 17, pp. 2857–2863, Sep. 2013.

[19] D. Mohammed, W. A. Khaleel, and A. Al-Janabi, "Tunable Q-switched erbium doped fiber laser based on metal transition oxide saturable absorber and refractive index characteristic of multimode interference effects," *Opt. Laser Technol.*, vol. 97, pp. 106–110, 2017.